

Article

A Novel Single-Turn Permanent Magnet Synchronous Machine for Electric Aircraft

Zeyu Cheng¹, Zhi Cao¹ , John T. Hwang² and Chris Mi^{1,*} ¹ Department of Electrical and Computer Engineering, San Diego State University, San Diego, CA 92182, USA² Department of Mechanical and Aerospace Engineering, University of California San Diego, La Jolla, CA 92023, USA

* Correspondence: cmi@sdsu.edu

Abstract: This paper proposes a novel multi-phase single-turn permanent magnet synchronous motor (MSPMSM) to meet the stringent requirements of electric aircraft, such as high power density, high torque, and low mass and volume. The MSPMSM features a unique single-turn winding configuration, which can reduce the coil overhang, increase the power density and torque, and reduce the weight of the motor in conventional multi-turn motors. The proposed MSPMSM is studied by the finite element method (FEM) and compared to a conventional PMSM with the same geometry and PM usage. The performance comparison results under different load conditions show that the proposed MSPMSM has higher torque and power density than the conventional motor.

Keywords: coil configuration; more electric aircraft; multiphase permanent magnet synchronous motor (PMSM); power density



Citation: Cheng, Z.; Cao, Z.; Hwang, J.T.; Mi, C. A Novel Single-Turn Permanent Magnet Synchronous Machine for Electric Aircraft. *Energies* **2023**, *16*, 1041. <https://doi.org/10.3390/en16031041>

Academic Editors: Ahmed Hafaifa, Obaid S. Alshammari and Abdelhamid Iratni

Received: 4 January 2023

Revised: 13 January 2023

Accepted: 14 January 2023

Published: 17 January 2023



Copyright: © 2023 by the authors. Licensee MDPI, Basel, Switzerland. This article is an open access article distributed under the terms and conditions of the Creative Commons Attribution (CC BY) license (<https://creativecommons.org/licenses/by/4.0/>).

1. Introduction

In the past decades, with climate change and environmental degradation becoming a growing concern, the transportation industry has been moving toward electrification. Electric vertical takeoff and landing (eVTOL) aircraft have been advocated as a feasible transportation solution for clean energy and traffic congestion in the future, especially if the electrified aircraft propulsion incorporates renewable energy, such as wind, solar, and tidal streams [1]. There has been significant interest in electric aircraft in recent years because of the advancement of batteries, motors, power converters, and materials. These trends provide opportunities and markets for the design of electric aircraft.

Urban air mobility (UAM) envisions a safe, ecological, and cost-effective air transportation system for transporting people and goods in densely populated area [2]. National Aeronautics and Space Administration (NASA) asserted that the required power density and efficiency for eVTOL aircraft could be 13 kW/kg and 96% or higher, respectively [3]. However, the dynamic performance of electric aircraft is highly sensitive to the mass of its components. Compared to conventional aircraft, the electrification of aircraft results in a significant increase in mass, which restricts the range of eVTOL aircraft. Therefore, to maximize range, eVTOL aircraft must meet stringent specifications for power density, power-to-weight ratio, efficiency, and reliability.

As a key component of the electric aircraft propulsion system, permanent magnet synchronous motors (PMSMs), brushless DC motors (BLDCs), and switched reluctance motors (SRMs) have been widely implemented due to their advantages, which are high efficiency and a wide operating speed range [4]. A scaling of normal motor topologies for electric aircraft was presented in [5]. PMSMs use high-energy-density magnet materials, such as NdFeB, to produce the high-density magnetic field along the air gap. These materials offer significant benefits for PMSMs, such as no excitation loss, high power density, high magnetic flux density, and high power factor. Therefore, PMSMs are getting more attention in electric aircraft [6].

Typically, a PMSM usually employs redundancy or fault tolerance optimization to improve reliability. The multi-phase motor is one of the most popular methods for achieving high reliability and high power density of the motor in electric aircraft and other applications. Compared with the conventional three-phase motor, the multi-phase motor has more flexible control strategies and winding distributions, which can improve the reliability of the system, optimize the magnetic flux density distribution, and provide higher power factor and torque density [7,8]. In [9], a multi-phase motor with asymmetric windings was proposed with the intent to minimize the cumulative loss over a single operational cycle to improve efficiency and reliability. A large amount of research has demonstrated that the multi-phase motor with symmetric windings can produce higher torque compared with the three-phase motor in the same geometry [10,11]. In addition, multiphase fault-tolerant motors were studied in [12–14], aiming to improve reliability and minimize the fault probabilities. A five-phase permanent magnet brushless motor driver was presented that allows the system to operate at rated torque and speed even when one or two phases are open or one phase is short-circuited.

The weight optimization of different motor topologies for electric aircraft propulsion was analyzed in [15], which showed that PMSMs have excellent power densities compared with other motors. In [16], weight was optimized with a two-stage motor design to achieve fault tolerance. In [17], researchers proposed integrated motor drives (IMDs) to improve the power density of electric motors, reduce the mass and volume of motors, and avoid excessive losses. The motor and converter were mounted on the integrated case and directly connected through the short wire cable. IMDs were developed in [18], which can provide high flexibility, more phases, and easier modular formation. A multi-phase IMD for electric aircraft application was proposed in [19], which considered the influence of different slot–pole ratios, cooling techniques, and skew angles of magnet poles on the performance of the motor.

In general, multiple turns of windings around the tooth create a stronger magnetic field, providing the electric motor with higher torque, speed, and the capacity to carry a heavier load without increasing the voltage. However, multi-turn coils have larger inductance and resistance in each phase than single-turn coils. Moreover, due to the winding distribution, there is a large portion of coils that hang outside of the stator and do not contribute to air-gap flux density and torque. Instead, this winding overhang increases phase resistance, leakage inductance, and the volume of the motor. In addition, multi-turn windings must account for the coil's insulation at high voltages and the utilization of slot fill. In order to overcome these problems, Zucker et al. proposed a novel topology, turnless structure (TLS), which places one conductor inside each slot and shortens one end of all the windings [20–22]. The turnless motor is comprised of modular units, and in each unit, a foldable three-phase inverter is directly connected to three-phase windings in the stator through a short wire cable to form a three-phase motor unit. This structure can reduce the mass and volume of the motor and increase the power density and efficiency, which makes it suitable for electric aircraft applications. However, the prior work did not investigate the overall performance of the turnless motor structure and its reliability. Therefore, this paper develops and presents a comprehensive analysis of the single-turn motor to prove the feasibility of a single-turn winding structure.

The multi-phase single-turn permanent magnet synchronous motor (MSPMSM) is proposed based on an extension of the turn-less motor in this paper. In the MSPMSM, compared with the conventional motor, a long, thick conductor is inserted into each slot to eliminate the detrimental impact of winding overhang, avoiding the excessive losses from external wire cable. The MSPMSM adopts a multi-phase winding distribution to produce high reliability, high torque, and high power density in comparison with the three-phase PMSM. In addition, the MSPMSM uses low-voltage, high-current SiC MOSFETs to maximize the utilization of each slot's area and reduce overall cost and power losses.

In Section 2, a multi-phase single-turn motor is demonstrated, which includes the evolution of a single-turn winding structure, the motor topology of the MSPMSM, the drive

system, the performance of the MSPMSM, and loss analysis. In Section 3, a conventional 20S8P double-layer PMSM is compared with the single-turn motor. The performance of both motors under a no-load condition and a load condition are shown in Section 3.

2. Multi-Phase Single-Turn Motor Topology

The application of interest in this paper is an electric air taxi capable of vertical takeoff and landing, which has strict requirements regarding efficiency, power density, affordability, safety, and emissions [23]. The electric aircraft can tilt and potentially retract the vertical-lift rotors due to the lower weight and volume of the electric motor, resulting in a higher cruise speed. Therefore, we proposed the single-turn motor with a novel winding distribution to reduce the size of the motor and maximize the slot-filling area, producing a higher torque density and power density to satisfy the requirements for eVTOL aircraft specifications.

2.1. Specification

Table 1 shows the main specifications of the MSPMSM. According to the high demand for electric aircraft, the mass and volume of the motor need to be reduced compared with the conventional motor. In the MSPMSM, a large current is injected into each slot while a low voltage is supplied. The rated speed for the single-turn motor is 6000 r/min.

Table 1. Main specifications of MSPMSM motor.

Parameters	Value
Peak Power, P	113 (kW)
Rated Speed, n	6000 (r/min)
Average Torque, T	191 (N·m)
Efficiency, η	>94 (%)
Voltage, U	48 (V)
Peak current, I	1500 (A)

2.2. Winding Distribution

The MSPMSM adopts a novel concept of winding distribution, turnless structure [20,21], as Figure 1 shows. The turnless structure can eliminate the external connections between each winding by severing the end terminal connection of distributed winding and shorting three adjacent conductors to generate a set of three shorted conductors in a wye configuration to reduce the volume of the motor. Moreover, each group of the TLS is connected directly to the inverter through a short wire cable to enhance power density further. Figure 1a shows the winding distribution of distributed winding. Figure 1b presents the turnless structure proposed by [21]. However, in the three-phase turnless motor, a large number of the TLS modules must be in parallel with each other and connect with a three-phase inverter at the end of every three conductors, achieving high reliability and continuity of the traveling magnetic field. This massively parallel structure has a stringent requirement for the MOSFET and redundancy of the system. When one of the three-phase inverters fails, the motor can not run normally. Hence, the multi-phase single-turn structure is proposed in this paper, as Figure 1c shows, to improve the reliability of electric motors and satisfy the high demand for eVTOL aircraft. There are five adjacent conductors whose end terminals are shorted together. Each set is energized through the five-phase sinusoidal current from the five-phase driver system, whose sum of the currents in the end terminals is always zero, so as to generate a traveling magnetic field that interacts with one pair of poles in the rotor. This multi-phase structure ensures that the motor can operate for a short period, even if any short or open circuits occur in any winding structure.

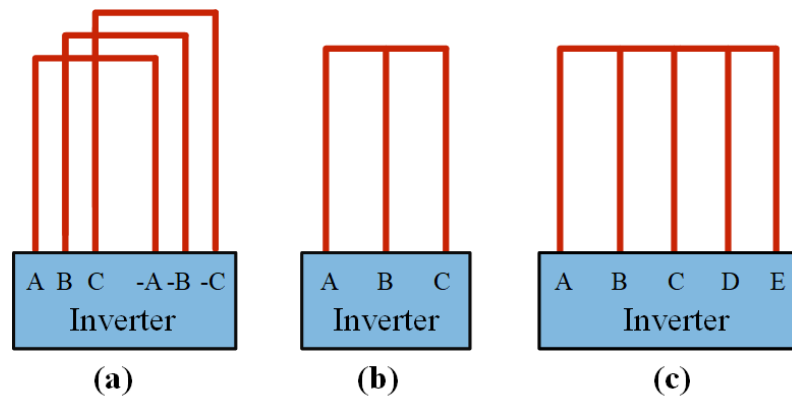


Figure 1. Winding distribution with (a) conventional distributed winding. (b) Three phase turnless structure. (c) Five-phase single-turn structure.

2.3. Motor Topology

In order to analyze the performance of the MSPMSM, a five-phase single-turn motor is compared to a traditional double-layer distributed five-phase PMSM in this section, which has the same main geometry dimensions as the five-phase single-turn motor, as shown in Table 2. Figure 2a presents the topology of the MSPMSM, a 20-slot, eight-pole stator with a TLS winding structure and an embedded radial magnetic pole rotor structure, resulting in low phase resistance, low leakage inductance, and higher power density. Figure 2b shows the topology of the traditional PMSM, which has a 20-slot, eight-pole stator with a double-layer winding distribution.

Table 2. Main geometry dimensions of five-phase single-turn motor and distributed PMSM.

Parameters	Value
Number of slots, Q	20
Number of poles, p	8
Number of phase, m	5
Stator outer diameter, D_1	406 (mm)
Stator inner diameter, D_i	254 (mm)
Effective length, L_{ef}	100 (mm)
Air gap, δ	1 (mm)
Shaft diameter, D_s	120 (mm)
Steel material	DW310
Magnet material	N30SH

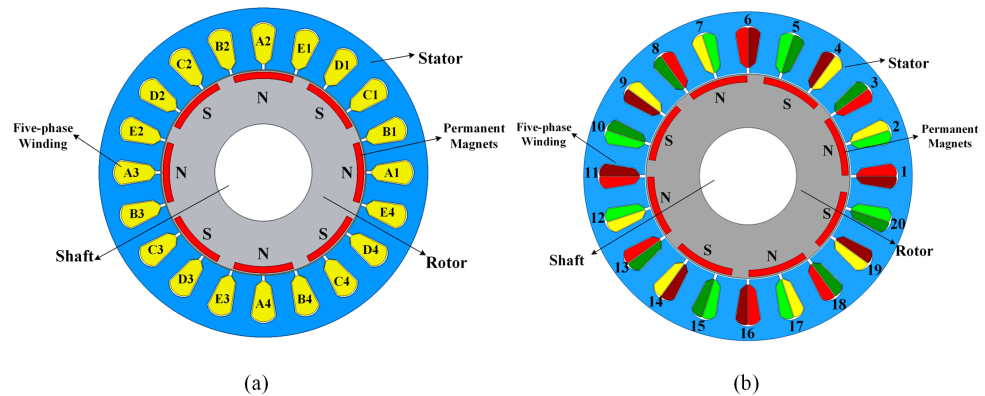


Figure 2. (a) Two dimensional topology of five-phase single-turn PMSM. (b) Two dimensional topology of conventional distributed five-phase PMSM.

Figure 3 demonstrates the motor winding connection for both types of motors. The five-phase single-turn windings are divided into four isolated groups of TLS structure. Each group connects with the five-phase inverter to improve the reliability of the system. The traditional five-phase distributed PMSM has four parallel branches in each phase, and the winding connection is shown in Figure 3b.

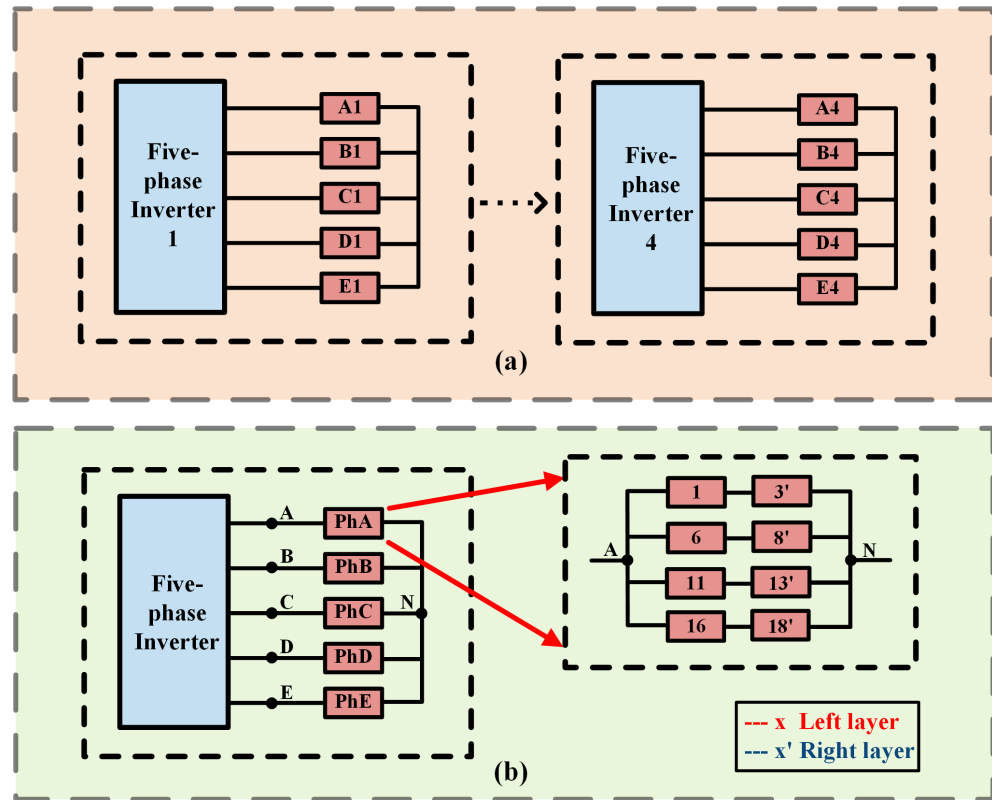


Figure 3. (a) Winding connection of five-phase single-turn PMSM. (b) Winding connection of distributed five-phase PMSM.

2.4. Driver Layout

The overall driver layout of a five-phase single-turn motor is shown in Figure 4. Maxwell 2D, Simplorer, and Simulink are used for coupled simulation. The power circuit is built in Simplorer software, and Maxwell 2D is used for magnetic analysis. The SPWM algorithm is adopted to produce a five-phases sinusoidal current waveform, and the control circuit is built in Simulink. Figure 5 shows the five-phase current waveform of SPWM.

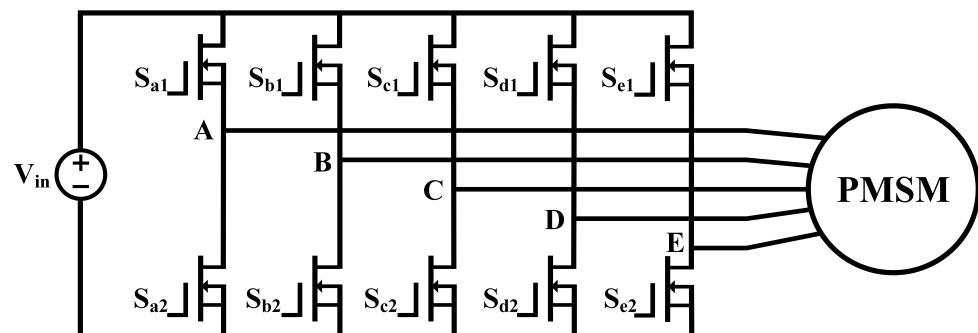


Figure 4. Schematic of five-phase single-turn motor driver circuit.

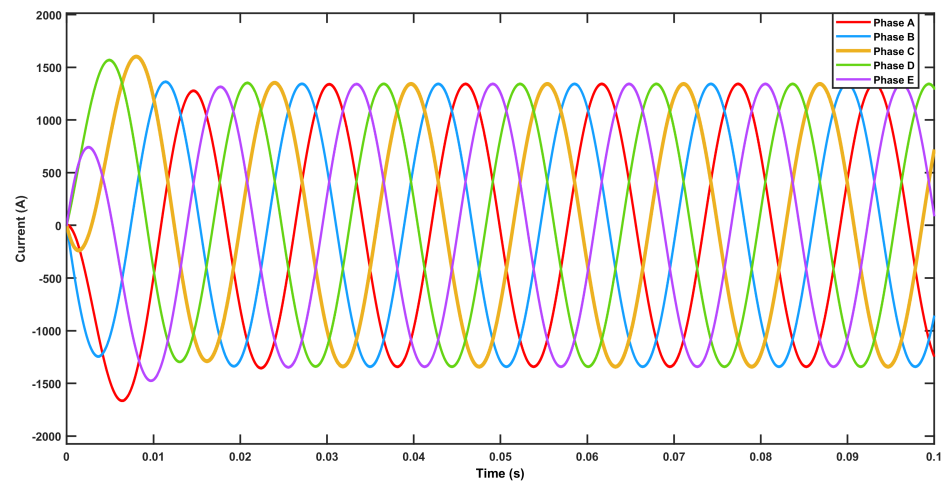


Figure 5. Schematic of five-phase single-turn motor driver circuit.

2.5. Loss Analysis

This section presents a loss analysis in order to obtain an overall performance of the single-turn structure. The total loss of the architecture includes iron loss, copper loss, mechanical loss, and MOSFET loss. The equations for loss analysis are shown below.

The Maxwell module analyzes copper losses, core losses, and mechanical losses of the MSPMSM. The core losses significantly contribute to the total losses, divided into two categories in the two-dimensional model: hysteresis loss and eddy current loss. Therefore, the total core loss is given by:

$$\begin{aligned}
 P_{\text{core}} &= \int_{\Gamma} (P_{\text{hys}} + P_{\text{ec}}) d\Gamma \cdot l_{ef} \\
 &= \int_{\Gamma} \sum_{n=1}^N [k_{\text{hys}} f_n \hat{B}_n^2 + k_{\text{ec}} (f_n \hat{B}_n)^2] d\Gamma \cdot l_{ef},
 \end{aligned} \tag{1}$$

where k_{hys} and k_{ec} represent the hysteresis loss coefficient and eddy current loss coefficient, respectively. \hat{B} is the peak magnetic flux density.

Copper losses and mechanical losses are expressed as follows:

$$\begin{aligned}
 P_{\text{cu}} &= m I^2 R_s \\
 P_{\text{m}} &= K_r \pi K_f \rho \omega^2 l_{ef} D_2^2,
 \end{aligned} \tag{2}$$

where R_s represents the phase resistance, K_r and K_f represent mechanical coefficients, and D_2 represents rotor diameter.

The mathematical model of MOSFET is shown as follows:

$$\begin{aligned}
 P_{\text{cond}} &= I_{\text{rms}}^2 R_{ds} \\
 P_{\text{switch}} &= \frac{C_{dd} V_{ds}^2 f_{sw}}{2} + \frac{V_{ds} I_{ds} (t_r + t_f) f_{sw}}{6},
 \end{aligned} \tag{3}$$

where D is the duty ratio of MOSFET, R_{ds} is the resistance of MOSFET, C_{dd} is the parasitic capacitance, V_{ds} is the drain to source voltage, I_{ds} is the drain current, f_{sw} is the switching frequency, and t_r and t_f are dead time at rising and falling.

3. Performance Comparison of MSPMSM with Different Motor Topology

To evaluate the performance of the MSPMSM, Ansoft Maxwell was used for multiple simulations with different phase and load conditions in this section, allowing for a comprehensive comparison of the performance of the two motors.

3.1. No Load Simulation

3.1.1. Comparison of Magnetic Field

Figure 6 shows the no-load magnetic flux density distribution of both winding structures. As can be seen, the magnetic bridges for both winding structures are saturated, which constrains the flux leakage. Moreover, the flux distribution of both winding is almost the same, indicating that single-turn winding can effectively utilize the magnet material as the conventional winding structure. The no-load magnetic flux density distribution along air gap B_{air} and its harmonic component are shown in Figure 7. The air gap flux distributions are almost the same since both winding structures have the same magnet thickness and distribution. The difference between winding structures does not affect the performance under no-load conditions.

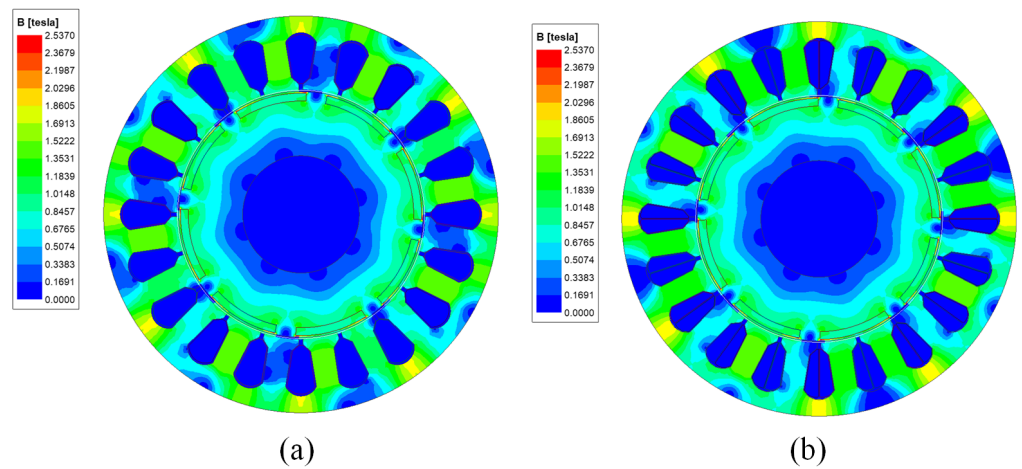


Figure 6. (a) Magnetic field of single-turn motor. (b) Magnetic field of double-layer motor.

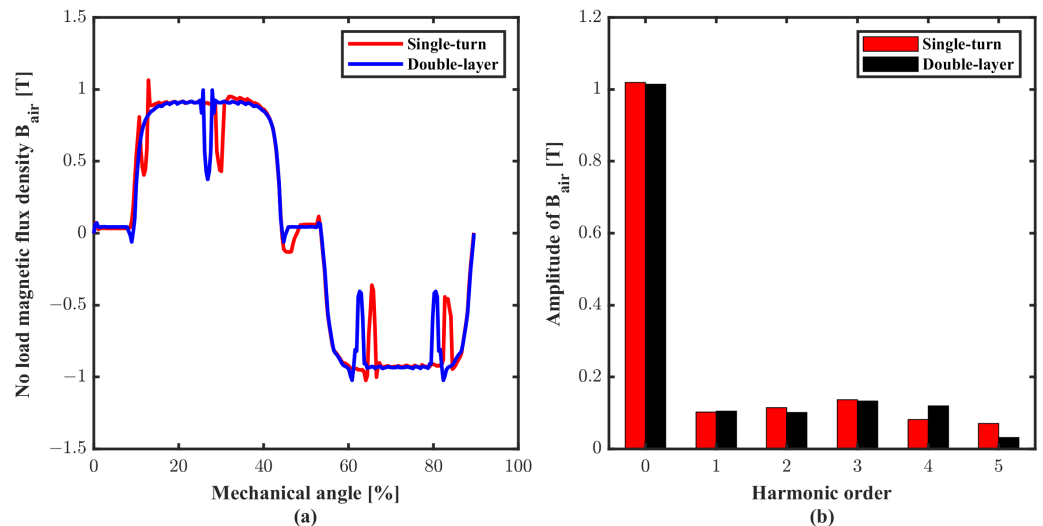


Figure 7. (a) No load air-gap magnetic flux density distribution. (b) Harmonic components of air-gap magnetic flux density.

3.1.2. Comparison of Back-EMF

The no-load back EMF waveform is presented in Figure 8. It can be seen that the back EMF amplitude of double-layer winding is significantly larger than the single-turn motor because multi-turns in each phase are wound around the tooth for double-layer winding distribution. In addition, the back EMF of a double-layer structure has a very low harmonic component, and the total harmonic distortion (THD) is 8.9%, which means double-layer winding has a high winding factor and better utilization of current excitation.

In contrast, the amplitude of back EMF for the single-turn motor is only 40 V since only a single-turn is present around the stator tooth. Furthermore, a single-turn motor has an abundant five-order harmonic component in the back EMF waveform, and the THD is 38.6%, which causes the flux linkage and back EMF to be distorted.

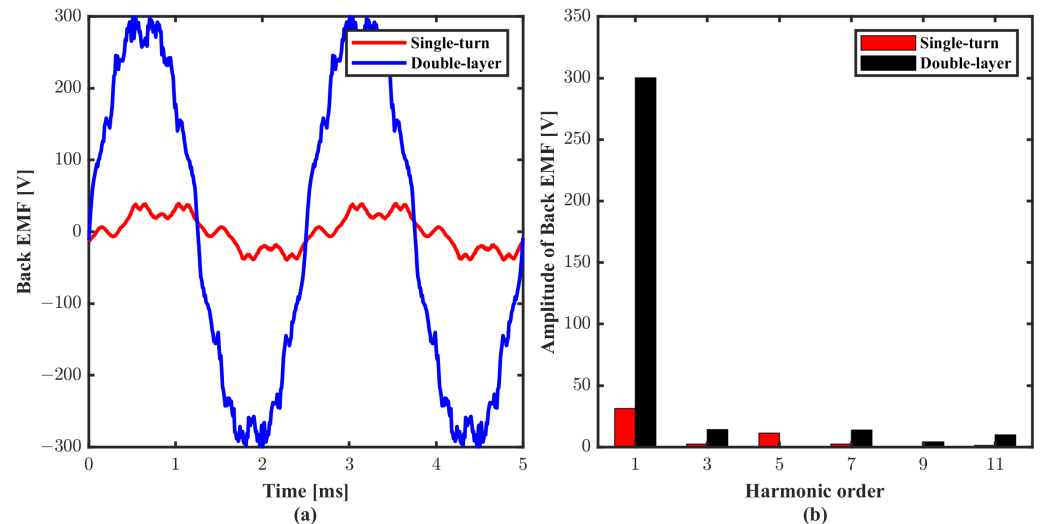


Figure 8. (a) The amplitude of Back EMF. (b) Harmonic content of Back EMF.

3.2. Load Simulation

The main specifications for the full load experiment are listed in Table 3.

Table 3. Main specifications for load experiment.

Parameters	Single-Turn	Double-Layer
Slots/Poles	20/8	20/8
Number of phase	5	5
Current density ($A \cdot mm^{-2}$)	4.7	4.7
Current (A)	1500	117
Speed (r/min)	6000	6000
Slot fill factor	1	0.78
Magnet thickness (mm)	8	8
Number of turns	1	5

3.2.1. Comparison of Torque

The motor for electric aircraft applications should have sufficient average torque to overcome the load and provide high accelerated performance in low-speed regions, low torque ripple, and cogging torque to reduce noise and vibration, as well as high power density and efficiency.

The single-turn motor can provide higher average torque than conventional motors since the special winding structure can support each phase of a single-turn winding energized with a higher current, leading to higher electromagnetic torque. In traditional multi-turn winding distributions, slot fill factor, the ratio of the cross-sectional area occupied by the conductors inserted into the slot to the total available area of the stator slot, is less than 100% theoretically, since there is inevitable useless area occupied by the conductor insulation layer, slot insulation layer, and gaps between conductors and slots. Therefore, the maximum possible output torque of the electric motor is not achievable due to the impact of the slot-fill factor and manufacturing technique. However, the impact of the slot-fill factor can be avoided in a single-turn winding distribution, as shown in Figure 9. Figure 9a shows the conductor distribution in the stator slot for double-layer winding distribution. The green rectangular area represents the slot insulation layer. Figure 9b

shows the conductor distribution for the single-turn winding structure. Since only one conductor is placed in each slot, the inevitable gap and conductor insulation layer between the conductors and slot can be ignored. This characteristic enables the single-turn motor to achieve higher torque and current via each slot with the same current density and slot area as conventional motors.

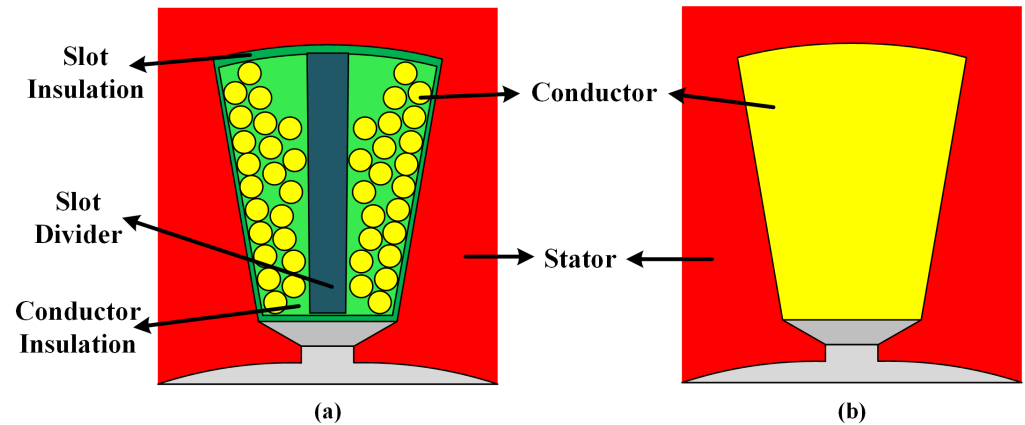


Figure 9. Winding distribution and illustration of slot fill factor. (a) Double-layer winding distribution. (b) Single-turn winding distribution.

Figure 10 shows the difference between the five-phase single-turn motor and the five-phase double-layer motor under full load conditions. The current amplitude for a single-turn motor is 1500A; the slot-fill factor is considered as 78% for double-layer winding. Therefore, the current amplitude for double-layer winding is only 1170 A to guarantee these motors operate under the same current density condition. As Figure 10 shows, the average torque of double-layer winding is 130.74 N·m, and the average torque of single-turn structure is 193.1 N·m under the same current density condition, which is 47.7% higher than traditional winding structure. In addition, the torque ripple of the single-turn winding structure is 40 N·m, which is around 20% of the output torque. Moreover, since the single-turn motor has a smaller volume, the five-phase single-turn motor will have a higher torque density compared with the five-phase double-layer motor.

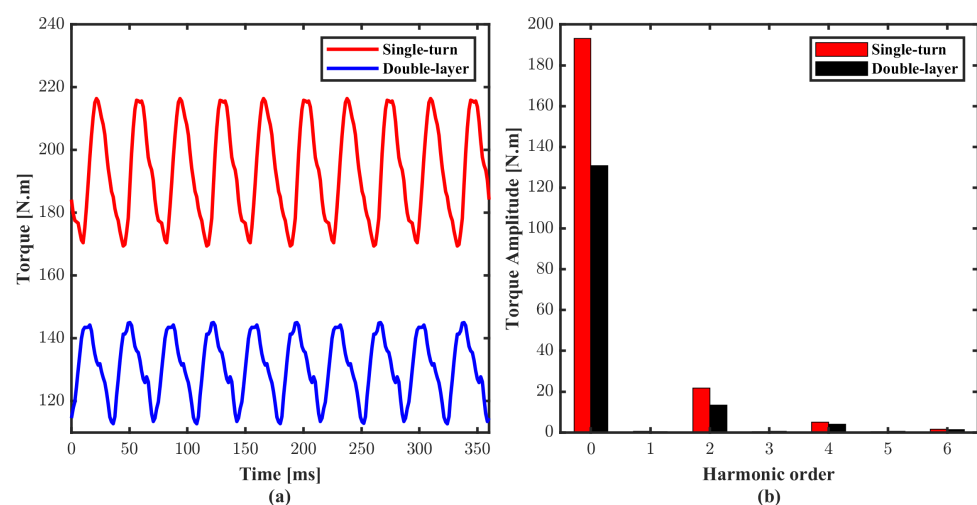


Figure 10. Torque Comparison between five-phase single-turn motor and double-layer motor. (a) Electromagnetic Torque. (b) Harmonic analysis.

Figure 11 shows the performance of both motors with different internal power angle under full load condition. The five-phase single-turn motor produces the largest torque,

193.1 N·m, when the internal power angle is equal to 60° ; the five-phase double-layer motor produces the largest torque, 143.538 N·m, when the internal power angle is equal to 45° .

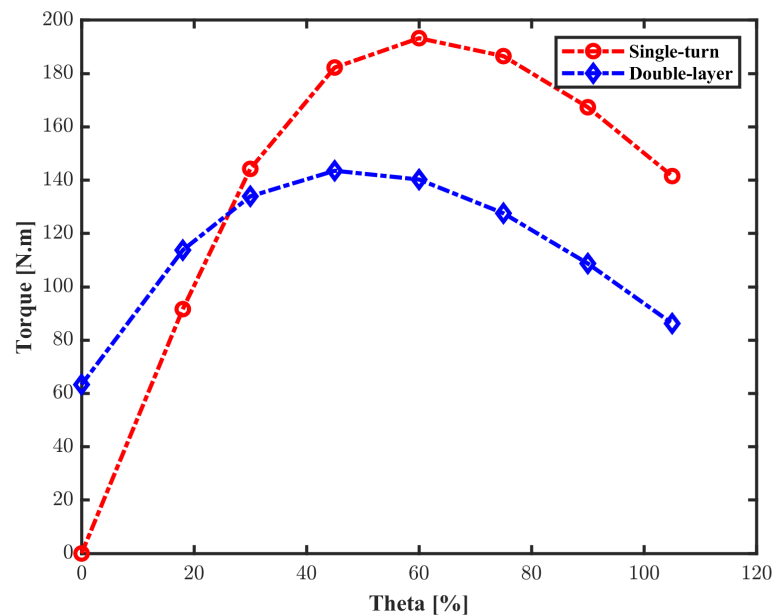


Figure 11. Winding distribution and illustration of slot fill factor.

3.2.2. Comparison of Magnetic field

As can be seen from the magnetic flux density cloud map in Figure 12, the magnetic flux densities for the two winding structures are similar. The highest magnetic flux density of the motor is located at the magnetic bridge, which is 2.53 T. The magnetic flux density near the magnetic bridge is saturated, which has a large resistance. The magnetic flux density through the tooth and yoke of the stator are 1.8 T and 1.6 T, respectively. The load magnetic flux density distribution along the air gap B_{air} and its harmonic component are shown in Figure 13. The fundamental amplitude of B_{air} for single-turn winding structure and double-layer winding structure are 1.068T and 1.0928T, respectively. The THD for both winding structures are 47.07% and 33.48%.

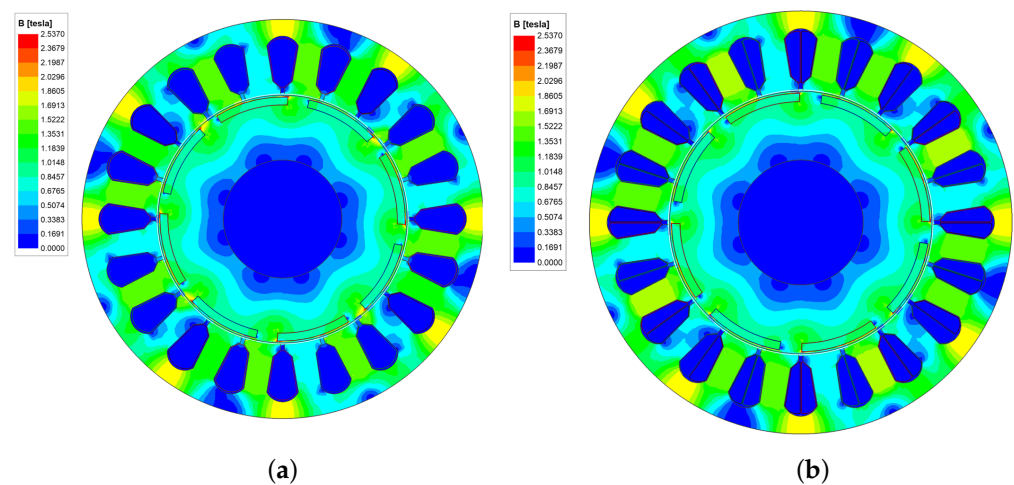


Figure 12. Magnetic flux density cloud map under full load condition. (a) Single-turn winding distribution. (b) Double-layer winding distribution.

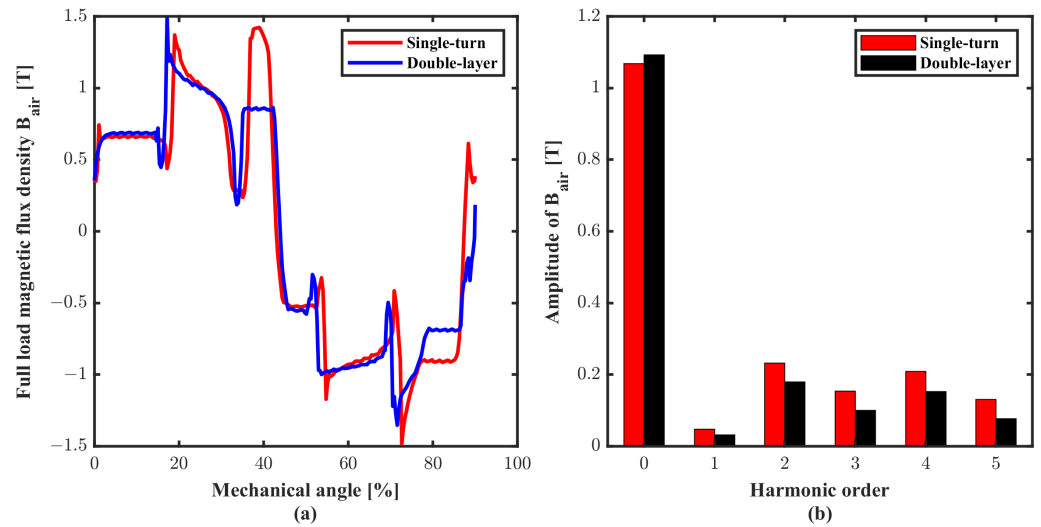


Figure 13. (a) Full load air-gap magnetic flux density distribution. (b) Harmonic components of air-gap magnetic flux density.

3.2.3. Comparison of EMF

Figure 14a shows the EMF waveform for both winding structures. Figure 14b presents the results of harmonic analysis. The winding factor for the single-turn motor is low, and the THD of EMF is 48.75%. The THD of EMF for the double-layer winding structure is 18.16%. The fundamental EMF amplitude for both winding structures are 33.56 V and 338.12 V, respectively.

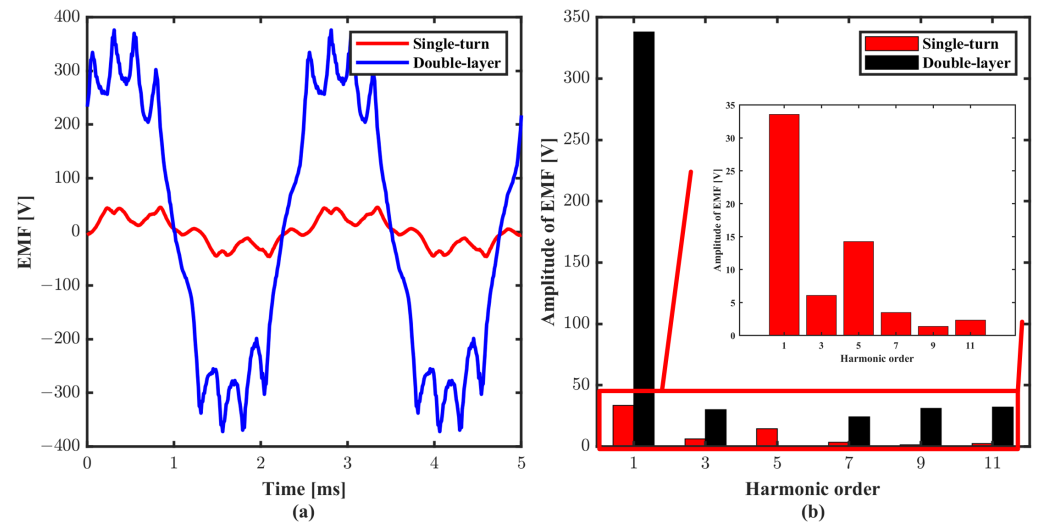


Figure 14. (a) The amplitude of EMF. (b) Harmonic analysis of EMF.

3.2.4. Comparison of Losses and Efficiency

As previously mentioned, efficiency is one of the key characteristics of electric motors for eVTOL aircraft. The method used to evaluate the efficiency is demonstrated in the previous section. The efficiency of PMSM is defined by the following:

$$\begin{aligned} \eta_m &= \frac{P_{em} - P_{iron}}{P_{em} + P_{copper}} \\ &= \frac{T_{em} * \Omega - T_o * \Omega}{T_{em} * \Omega + P_{copper}} \end{aligned} \quad (4)$$

where P_{em} is electromagnetic power, T_{em} is electromagnetic torque, T_o is iron loss torque, Ω is rotor speed, P_{copper} is the five-phase copper loss, and P_{iron} is iron loss of stator and rotor, which included the hysteresis loss and eddy-current loss. In addition, the efficiency of the whole system is also considered by:

$$\begin{aligned}\eta_s &= \frac{P_{em} - P_{iron}}{P_{em} + P_{copper} + \sum P_{mos}} \\ &= \frac{T_{em} * \Omega - T_o * \Omega}{T_{em} * \Omega + P_{copper} + P_{cond} + P_{switch}}\end{aligned}\quad (5)$$

where P_{cond} and P_{switch} are conduction and switching loss of MOSFET, respectively.

Figure 15 shows the losses for the 20S8P single-turn motor and 20S8P distributed double-layer motor under load conditions. The iron loss for both winding structures is 2204 W and 1460 W, respectively. The copper loss is 1768 W and 387 W, respectively. Since the single-turn motor has a larger current energized into each slot than the double-layer winding structure, the single-turn motor should have a larger copper loss than the double-layer winding structure. The efficiency of PMSM, η_m , for both winding structures, is 95.9% and 97.6%.

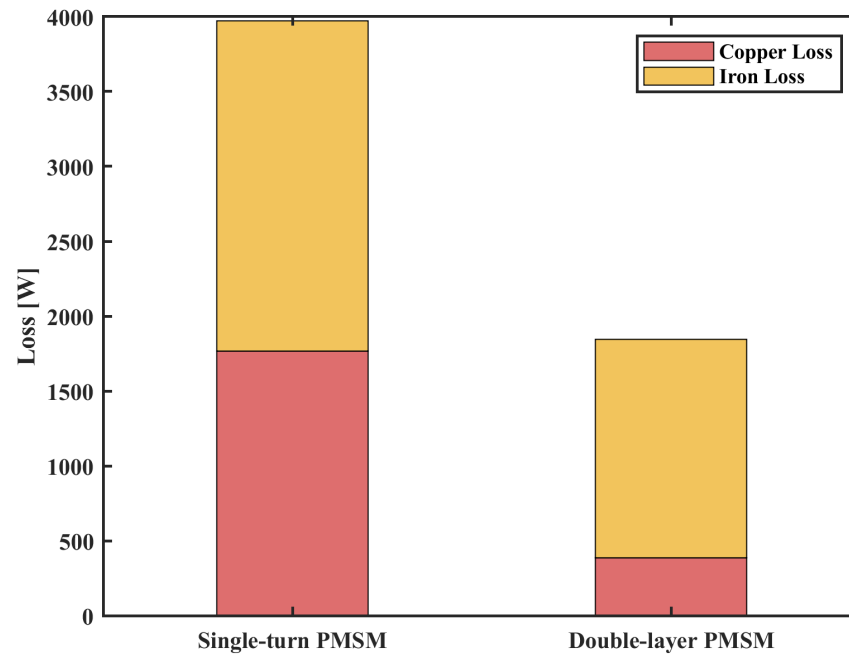


Figure 15. Losses for single-turn winding structure and conventional winding structure under load condition.

The specifications of MOSFET for single-turn motor and double-layer motor are shown in Table 4. In order to reduce the conduction loss of the single-turn motor, three MOSFETs are parallel to divide the drain to source current through each MOSFET. The losses of MOSFET are calculated based on Equation (3). The conduction loss for the single-turn and double-layer winding structures is 5981 W and 889.1 W. The switching loss is 769 W and 86 W, respectively. The efficiency of the system, η_s , for both winding structures, is 90.6% and 96.4%.

Table 4. Specifications for MOSFETs.

Parameters	Single-Turn PMSM	Double-Layer PMSM
R_{ds}	1.6 (m Ω)	13 (m Ω)
Maximum V_{ds}	100 (V)	750 (V)
Maximum I_{ds}	860 (A)	140 (A)
f_{sw}	20 (kHz)	20 (kHz)
t_r	270 (ns)	43 (ns)
t_f	175 (ns)	14 (ns)
C_{dd}	22 (nF)	475 (pF)
Cost for each MOSFET	362 (\$)	49.9 (\$)

4. Conclusions

This paper proposes a novel multi-phase single-turn motor topology featured by a unique single-turn winding structure for power density and torque density enhancement for eVTOL aircraft application. The proposed winding structure aims to eliminate the influence of winding coil overhang, thereby reducing the volume of the motor and increasing the power density. Special attention has been paid to the single-turn winding structure that makes the highest utilization of slot area possible compared with that of the conventional winding distribution, which leads to higher current energized into each slot and further produces higher torque.

The performance of the five-phase single-turn motor and that of the five-phase double-layer motor are compared in different loading conditions, investigating the advantages and unique problems of the MSPMSM. The losses and efficiency analysis of the whole system is presented in this paper. It has been found that the torque produced by the proposed winding structure is 47.7% higher than the conventional motor with the same current density. In addition, the single-turn motor has similar flux density distribution and magnetic performance to the conventional motor. Moreover, the efficiency of the single-turn motor is slightly less than the conventional motor. However, due to the large current characteristic, the system efficiency of the single-turn motor is 5.8% less than the conventional motor since the higher conduction loss of MOSFETs is inevitable, which leads to the stringent requirement for MOSFET specifications.

The proposed MSPMSM has higher torque density, higher power density, and lower mass and volume than the conventional motor. However, the proposed concept still has much potential for advancement. There are abundant five-order harmonic components in the EMF, which lead to large distortion in the flux linkage and EMF. It is possible to utilize these five-harmonic components to further improve the output torque. Furthermore, the optimization of the proposed motor to reduce the influence of harmonic components will be treated in the future.

Author Contributions: Conceptualization, Z.C. (Zeyu Cheng) and C.M.; methodology, Z.C. (Zeyu Cheng); software, Z.C. (Zeyu Cheng); validation, Z.C. (Zeyu Cheng) and Z.C. (Zhi Cao); formal analysis, Z.C. (Zeyu Cheng); investigation, Z.C. (Zeyu Cheng); resources, Z.C. (Zeyu Cheng); data curation, Z.C. (Zeyu Cheng); writing—original draft preparation, Z.C. (Zeyu Cheng); writing—review and editing, Z.C. (Zhi Cao), C.M. and J.T.H.; visualization, C.M. and J.T.H.; supervision, C.M.; project administration, C.M.; funding acquisition, C.M. All authors have read and agreed to the published version of the manuscript.

Funding: This material is based on work supported by NASA under award No. 80NSSC21M0070.

Data Availability Statement: Not applicable.

Conflicts of Interest: The authors declare no conflict of interest.

References

1. Patterson, M.D.; Antcliff, K.R.; Kohlman, L.W. A proposed approach to studying urban air mobility missions including an initial exploration of mission requirements. In Proceedings of the Annual Forum and Technology Display, Phoenix, AZ, USA, 14–17 May 2018.
2. Reiche, C.; Goyal, R.; Cohen, A.; Serrao, J.; Kimmel, S.; Fernando, C.; Shaheen, S. Urban Air Mobility Market Study. 2018. Available online: <https://doi.org/10.7922/G2ZS2TRG> (accessed on 21 November 2018).
3. Hathaway, M.D.; Rosario, R.D.; Madavan, N.K. NASA fixed wing project propulsion research and technology development activities to reduce thrust specific energy consumption. In Proceedings of the Joint Propulsion Conference and Exhibit, San Jose, CA, USA, 14–17 July 2013.
4. Cao, W.; Mecrow, B.C.; Atkinson, G.J.; Bennett, J.W.; Atkinson, D.J. Overview of Electric Motor Technologies Used for More Electric Aircraft (MEA). *IEEE Trans. Ind. Electron.* **2012**, *59*, 3523–3531. <https://doi.org/10.1109/TIE.2011.2165453>.
5. Wheeler, P.; Sirimanna, T.S.; Bozhko, S.; Haran, K.S. Electric/Hybrid-Electric Aircraft Propulsion Systems. *Proc. IEEE* **2021**, *109*, 1115–1127. <https://doi.org/10.1109/JPROC.2021.3073291>.
6. Zhang, X.; Bowman, C.L.; O'Connell, T.C.; Haran, K.S. Large electric machines for aircraft electric propulsion. *IET Electr. Power Appl.* **2018**, *12*, 767–779. <https://doi.org/10.1049/iet-epa.2017.0639>.
7. Pavithran, K.; Parimelalagan, R.; Krishnamurthy, M. Studies on inverter-fed five-phase induction motor drive. *IEEE Trans. Power Electron.* **1988**, *3*, 224–235. <https://doi.org/10.1109/63.4353>.
8. Guzman, H.; Duran, M.J.; Barrero, F.; Bogado, B.; Toral, S. Speed Control of Five-Phase Induction Motors With Integrated Open-Phase Fault Operation Using Model-Based Predictive Current Control Techniques. *IEEE Trans. Ind. Electron.* **2014**, *61*, 4474–4484. <https://doi.org/10.1109/TIE.2013.2289882>.
9. Zhao, T.; Wu, S.; Cui, S. Multiphase PMSM With Asymmetric Windings for More Electric Aircraft. *IEEE Trans. Transp. Electrif.* **2020**, *6*, 1592–1602. <https://doi.org/10.1109/TTE.2020.2997609>.
10. Casadei, D.; Mengoni, M.; Tani, A.; Serra, G.; Zarri, L. Torque maximization in high-torque density multiphase drives based on induction motors. In Proceedings of the 2010 IEEE Energy Conversion Congress and Exposition, Atlanta, GA, USA, 12–16 September 2010; pp. 3896–3902. <https://doi.org/10.1109/ECCE.2010.5617775>.
11. Xu, H.; Toliyat, H.; Petersen, L. Rotor field oriented control of five-phase induction motor with the combined fundamental and third harmonic currents. In Proceedings of the APEC 2001. Sixteenth Annual IEEE Applied Power Electronics Conference and Exposition (Cat. No.01CH37181), Anaheim, CA, USA, 4–8 March 2001; Volume 1, pp. 392–398. <https://doi.org/10.1109/APEC.2001.911677>.
12. Villani, M.; Tursini, M.; Fabri, G.; Castellini, L. High Reliability Permanent Magnet Brushless Motor Drive for Aircraft Application. *IEEE Trans. Ind. Electron.* **2012**, *59*, 2073–2081. <https://doi.org/10.1109/TIE.2011.2160514>.
13. Villani, M.; Tursini, M.; Fabri, G.; Castellini, L. Multi-phase fault tolerant drives for aircraft applications. In Proceedings of the Electrical Systems for Aircraft, Railway and Ship Propulsion, Bologna, Italy, 19–21 October 2010; pp. 1–6. <https://doi.org/10.1109/ESARS.2010.5665246>.
14. Arumugam, P.; Barater, D.; Hamiti, T.; Gerada, C. Winding concepts for ultra reliable electrical machines. In Proceedings of the IECON 2014—40th Annual Conference of the IEEE Industrial Electronics Society, Dallas, TX, USA, 29 October–1 November 2014; pp. 959–964. <https://doi.org/10.1109/IECON.2014.7048617>.
15. Anderson, A.D.; Renner, N.J.; Wang, Y.; Agrawal, S.; Sirimanna, S.; Lee, D.; Banerjee, A.; Haran, K.; Starr, M.J.; Felder, J.L. System Weight Comparison of Electric Machine Topologies for Electric Aircraft Propulsion. In Proceedings of the 2018 AIAA/IEEE Electric Aircraft Technologies Symposium (EATS), Cincinnati, OH, USA, 12–14 July 2018; pp. 1–16.
16. Galea, M.; Buticchi, G.; Empringham, L.; de Lillo, L.; Gerada, C. Design of a High-Force-Density Tubular Motor. *IEEE Trans. Ind. Appl.* **2014**, *50*, 2523–2532. <https://doi.org/10.1109/TIA.2014.2300190>.
17. Brown, N.R.; Jahns, T.M.; Lorenz, R.D. Power Converter Design for an Integrated Modular Motor Drive. In Proceedings of the 2007 IEEE Industry Applications Annual Meeting, New Orleans, LA, USA, 23–27 September 2007; pp. 1322–1328. <https://doi.org/10.1109/O7IAS.2007.205>.
18. Wang, J.; Li, Y.; Han, Y. Integrated Modular Motor Drive Design With GaN Power FETs. *IEEE Trans. Ind. Appl.* **2015**, *51*, 3198–3207. <https://doi.org/10.1109/TIA.2015.2413380>.
19. Wu, S.; Tian, C.; Zhao, W.; Zhou, J.; Zhang, X. Design and Analysis of an Integrated Modular Motor Drive for More Electric Aircraft. *IEEE Trans. Transp. Electrif.* **2020**, *6*, 1412–1420. <https://doi.org/10.1109/TTE.2020.2992901>.
20. Liu, C.; Paul, K.; Zucker, O. Experimental Demonstrations of a Representative Motor and Linear Actuator Using Controlled Turn-Less Structure Arrays Motors (CTM). Available online: <https://indi.to/87fLM> (accessed on 6 June 2018).
21. Zucker, O.S.; Blumenau, L.; Liu, C.; Yu, P.K. New High Specific Power Motor Technology for All-Electric Class III UAVs. In Proceedings of the 2018 IEEE International Power Modulator and High Voltage Conference (IPMHVC), Jackson, WY, USA, 3–7 June 2018; pp. 58–63. <https://doi.org/10.1109/IPMHVC.2018.8936760>.

22. Zucker, O. Electric Motor/Generator With Multiple Individually Controlled Turn-Less Structures. U.S. Patent Application 13/844,347, 28 November 2013.
23. NASA. Strategic Implementation Plan 2019 Update. Technical Report. 2019. Available online: <https://www.nasa.gov/sites/default/files/atoms/files/sip-2019-v7-web.pdf> (accessed on 14 June 2020).

Disclaimer/Publisher's Note: The statements, opinions and data contained in all publications are solely those of the individual author(s) and contributor(s) and not of MDPI and/or the editor(s). MDPI and/or the editor(s) disclaim responsibility for any injury to people or property resulting from any ideas, methods, instructions or products referred to in the content.